Mechanics of Advanced Composite Structures

Journal homepage: https://macs.semnan.ac.ir/

Semnan University

ISSN: 2423-7043

Research Article

Numerical Estimation of the Effective Mechanical Properties (EMP) of Steel AISI 4340 Fiber-Reinforced Concrete

Nasserdine Oudni [a*], Mohamed Said Boutaani [b], Youcef Bouafia [c] Ahmed Laichaoui [d]

[a] *Department of Civil Engineering, Faculty of Technology, University of Bejaia, 06000 Bejaia, Algeria.*
[b] *Common Core of Science and Technology, Faculty of Technology, University of Batna 2, 05000 Batna, Algeria.*
[c] *Department of Civil Engineering, Mouloud Mammeri University, 15000, Tizi-Ouzou, Algeria*
[d] *Laboratory of Construction Engineering and Architecture, University of Bejaia, 06000 Bejaia, Algeria*

ARTICLE INFO

Article history:

Received:
Revised:
Accepted:

Keywords:

Homogenization;
Composite;
Effective Properties;
RVE;
Random distribution;

ABSTRACT

This study aims to estimate the effective mechanical properties (EMP) of a composite material consisting of two phases: a concrete matrix and randomly distributed cylindrical fiber reinforcements. To determine the composite's effective mechanical properties, several key parameters are considered, including the fiber volume fraction, fiber geometry (expressed as the length-to-diameter ratio), and the void volume fraction. The voids are modeled as spherical inclusions, randomly dispersed within the matrix phase only, with strict non-intersection constraints, ensuring they do not overlap or touch the fibers. This configuration reflects realistic entrapped air porosity while preserving the integrity of the fiber-matrix interface. The effective elastic properties are estimated using a numerical homogenization procedure based on the finite element method (FEM) and the representative volume element (RVE) concept. Periodic boundary conditions (PBC) are applied to ensure representativeness, and a progressive mesh refinement strategy is employed, with a finer mesh around the inclusions, to balance accuracy and computational efficiency. The 3D fiber distributions are generated using a custom Python 3.9 script that enforces non-overlapping conditions between fibers, thereby preventing interpenetration during RVE construction.

1. Introduction

Currently, global industrial demand for natural resources is substantial, leading to their overexploitation. To mitigate resource depletion and promote sustainable development, the construction sector increasingly incorporates waste materials—such as mineral by-products, agricultural residues, and synthetic industrial waste—into building products. This approach reduces the environmental footprint of construction while conserving finite natural resources. Concrete and steel are the most widely used materials in civil engineering. To enhance sustainability, numerous studies have explored the incorporation of recycled or bio-based constituents into construction composites. For instance, concrete can be produced using recycled aggregates [1–3], while steel machining chips have been repurposed as reinforcement in fiber-reinforced concrete [4, 5]. Beyond conventional materials, natural fibers such as rice straw [6], bamboo [7], hemp [8, 9], palm [10, 11], and flax [12] are increasingly

* **Corresponding author.**
E-mail address: *nasserdine.oudni@univ-bejaia.dz*

Cite this article as:
Oudni, N. Boutaani, M.S. Laichaoui, A., 2025. Numerical Estimation of the Effective Mechanical Properties (EMP) of Steel AISI 4340 Fiber-Reinforced Concrete. *Mechanics of Advanced Composite Structures*, 12(1), pp. xx-xx
https://doi.org/10.22075/MACS.2024.39315.2050

embedded—either as short or long fibers—into cementitious matrices to develop eco-friendly composites. Recent research on innovative lattice architectures—such as those based on octagonal bipyramids, double octagonal bipyramids, and quadrilateral bipyramids—combines advanced analytical modeling, numerical simulations, and experimental validation to optimize mechanical performance and energy absorption capacity. Additionally, other studies propose the use of innovative materials, such as functionally graded structures or metamaterials—particularly graded auxetic architectures—to mitigate stress shielding in implants [18]. This research is crucial for enhancing the strength and durability of existing structures and supporting the development of new materials that meet the demands of modern construction, thereby promoting the adoption of sustainable solutions in the built environment.

The study aims to determine the effective elastic properties—namely, the longitudinal Young's modulus, shear modulus, and Poisson's ratio—of steel fiber-reinforced concrete at the mesoscale using numerical homogenization applied to a three-dimensional representative volume element (RVE) under periodic boundary conditions. This approach directly addresses the current lack of mesoscale homogenized elastic data for concrete-based composites incorporating realistic fiber distributions. To this end, several parameters are varied, including the fiber volume fraction, fiber geometry (expressed as the length-to-diameter ratio), and void volume fraction. The resulting effective properties differ from those of the individual constituents, which typically comprise a matrix and reinforcing inclusions (e.g., fibers). This study considers a two-phase composite material composed of steel fibers embedded in a concrete matrix, with both constituents assumed to be homogeneous. The homogenization process employs a mechanics-based modeling framework to replace a heterogeneous material—represented by an RVE—with an equivalent homogeneous medium possessing effective properties [19–23]. Such heterogeneity may arise from multiple sources, including aggregates of varying sizes and shapes, spatial variations in the cementitious matrix, or the presence of pores and voids across different length scales [24, 25]. Because they rely on a precise or approximate representation of the microstructure, homogenization approaches are also referred to as micromechanical models [26–28]. To characterize an isotropic material, two independent elastic constants are required, typically Young's modulus (E) and Poisson's ratio (ν), though other valid pairs may be used depending on the context. The elastic constants of a material are inherently interrelated; for isotropic media, the shear modulus (G) is not independent but derives from E and ν. In this work, the numerical results are presented graphically and compared with predictions from several analytical models [29–33] for validation. Analytical models, however, exhibit well-documented limitations, particularly when applied to complex multiphase systems:

(i) they typically rely on idealized microstructural assumptions—such as dilute distributions, perfect interfacial bonding, and ellipsoidal or spherical inclusions—which fail to capture the true geometric complexity, fiber agglomeration, or interfacial defects present in real composites;

(ii) most two- or three-phase analytical schemes are unable to simultaneously account for competing heterogeneities, such as stiff fibers and compliant pores;

(iii) they neglect local fluctuations in mechanical fields and stress concentrations, which critically influence the effective material response;

(iv) Finally, these models are generally derived under linear elastic assumptions and provide no description of post-peak mechanisms, such as damage evolution, interfacial debonding, or plasticity.

This study is divided into two parts. In the first part, the effective mechanical properties (EMPs) of the composite—comprising concrete and steel fibers—are determined in the absence of pores. In the second part, the influence of porosity is investigated by incorporating spherical voids at varying volume fractions into the composite, and the resulting EMPs are estimated accordingly. While the numerical framework is standard, the contribution focuses on the combined treatment of fibers and voids within a 3D RVE and on the analysis of their coupled influence on effective elastic properties through a systematic parametric study.

2. Modeling of the RVE Model

Generating a representative volume element (RVE) with randomly distributed fibers is among the most challenging steps in micromechanical modeling. This difficulty arises from the complex microstructure and the requirement that fibers must not overlap—a constraint that necessitates sophisticated placement algorithms, such as random sequential addition (RSA) or other advanced packing strategies [34]. The fibers are positioned within the RVE matrix using a Python 3.9 script, as shown in Figure 1. Two non-overlapping constraints are imposed: (i) no contact between fibers, and (ii) no contact between the fibers and the RVE boundaries. The

fiber volume fraction is given by the following formula [35]:

$$V_f = \frac{N, \pi, r^2, h}{L^3} \quad (1)$$

where V_f is the fiber volume fraction, N is the number of fibers, r is the fiber radius, h is the fiber length, and L is the cell length.

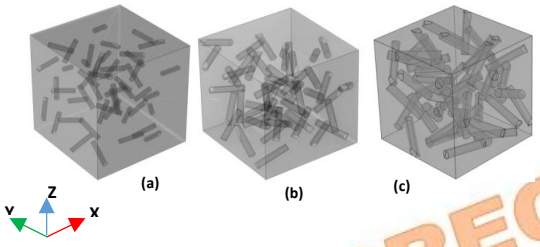

Fig. 1. RVEs with fiber volume fractions of (a) 2%, (b) 5%, and (c) 10%.

3. Numerical Homogenization

The material under study is a two-phase composite, assumed homogeneous at the phase level: a continuous concrete matrix embedding randomly distributed, discontinuous cylindrical steel fibers. The three-dimensional representative volume element (RVE) serves as the elementary cell of a periodic mesostructure for homogenization purposes.

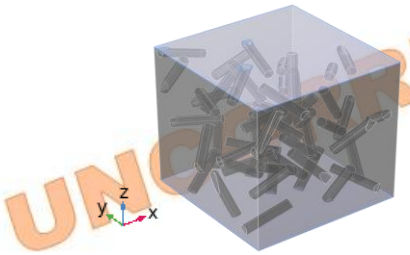

Fig. 2. RVE containing randomly distributed fibers.

Homogenization is performed to determine the effective mechanical response of the representative volume element (RVE) under applied loading, from which the effective mechanical properties of the composite are derived. These effective properties are assumed to represent the macroscopic behavior of the heterogeneous material at the structural scale. Composites reinforced with randomly distributed fibers—such as those shown in Figure 2—typically exhibit statistically isotropic behavior at the mesoscale, provided the fiber distribution is sufficiently uniform, and the RVE is representative. In contrast, composites with fibers arranged in an ordered pattern (e.g., a hexagonal lattice) and aligned in a single direction display transversely isotropic properties. In the present study, the steel fibers are randomly oriented and positioned, leading to macroscopically isotropic effective properties at the mesoscopic scale.

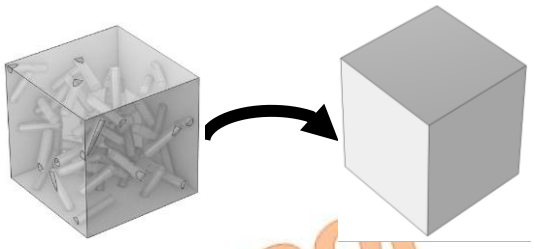

Fig. 3. RVE used for numerical homogenization.

Isotropic materials—such as steel and aluminum—are widely used in engineering applications because their mechanical properties are independent of direction. The elastic behavior of isotropic materials is fully described by two independent constants; the most common pair is Young's modulus E and Poisson's ratio ν. Alternative pairs, such as E and the shear modulus G, may also be used, but they are not independent: for isotropic materials, these constants are related through the well-known identity. This interdependence is embedded in the generalized Hooke's law, which defines the linear stress–strain relationship for isotropic media as follows [36, 37]:

$$\sigma = C\varepsilon \quad (2)$$

where C is the stiffness matrix (or the elastic par ameters matrix), σ and ε are the stress and strain vectors given, respectively, by:

$$\{\sigma_x \ \sigma_y \ \sigma_z \ \tau_{yz} \ \tau_{zx} \ \tau_{xy}\}^t \quad (3)$$

$$\{\varepsilon_x \ \varepsilon_y \ \varepsilon_z \ \gamma_{yz} \ \gamma_{zx} \ \gamma_{xy}\}^t \quad (4)$$

where σ_x, σ_y and σ_z are the normal stress components in x, y and z directions, τ_{yz}, τ_{zx} and τ_{xy} is the shear stress in $(y-z)$, $(z-x)$ and $(z-y)$ plans, respectively. ε_x, ε_y and ε_z are the normal stress components in x, y and z directions, γ_{yz}, γ_{zx} and γ_{xy} are the shear strains in $(y-z)$, $(z-x)$ and $(z-y)$ plans, respectively.

Although the microstructure of composites with randomly distributed reinforcements is inherently non-periodic, their effective elastic properties are commonly estimated by analyzing a statistically representative periodic unit cell (Figure 3) and volume-averaging the stiffness tensor C (Equation (5)). When the fiber distribution is sufficiently random and uniform, the resulting effective behavior may be approximated as isotropic.

$$C = \begin{bmatrix} C_{11} & C_{12} & C_{12} & 0 & 0 & 0 \\ C_{12} & C_{11} & C_{12} & 0 & 0 & 0 \\ C_{12} & C_{12} & C_{11} & 0 & 0 & 0 \\ 0 & 0 & 0 & \frac{C_{11}-C_{12}}{2} & 0 & 0 \\ 0 & 0 & 0 & 0 & \frac{C_{11}-C_{12}}{2} & 0 \\ 0 & 0 & 0 & 0 & 0 & \frac{C_{11}-C_{12}}{2} \end{bmatrix} \quad (5)$$

For a linear elastic material under a three-dimensional stress state, Hooke's law states that the strain at a point is a linear function of the stress components. In Cartesian coordinates (x, y, z), the stress–strain relationship is expressed as:

$$\begin{bmatrix} \varepsilon_x \\ \varepsilon_y \\ \varepsilon_z \\ \gamma_{yz} \\ \gamma_{zx} \\ \gamma_{xy} \end{bmatrix} = \begin{bmatrix} \frac{1}{E} & -\frac{v}{E} & -\frac{v}{E} & 0 & 0 & 0 \\ -\frac{v}{E} & \frac{1}{E} & -\frac{v}{E} & 0 & 0 & 0 \\ -\frac{v}{E} & -\frac{v}{E} & \frac{1}{E} & 0 & 0 & 0 \\ 0 & 0 & 0 & \frac{1}{G} & 0 & 0 \\ 0 & 0 & 0 & 0 & \frac{1}{G} & 0 \\ 0 & 0 & 0 & 0 & 0 & \frac{1}{G} \end{bmatrix} \begin{bmatrix} \sigma_x \\ \sigma_y \\ \sigma_z \\ \tau_{yz} \\ \tau_{zx} \\ \tau_{xy} \end{bmatrix} \quad (6)$$

$$\begin{bmatrix} \sigma_x \\ \sigma_y \\ \sigma_z \\ \tau_{yz} \\ \tau_{zx} \\ \tau_{xy} \end{bmatrix} = \begin{bmatrix} \frac{E(1-v)}{(1-2v)(1+v)} & \frac{vE}{(1-2v)(1+v)} & \frac{vE}{(1-2v)(1+v)} & 0 & 0 & 0 \\ \frac{vE}{(1-2v)(1+v)} & \frac{E(1-v)}{(1-2v)(1+v)} & \frac{vE}{(1-2v)(1+v)} & 0 & 0 & 0 \\ \frac{vE}{(1-2v)(1+v)} & \frac{vE}{(1-2v)(1+v)} & \frac{E(1-v)}{(1-2v)(1+v)} & 0 & 0 & 0 \\ 0 & 0 & 0 & G & 0 & 0 \\ 0 & 0 & 0 & 0 & G & 0 \\ 0 & 0 & 0 & 0 & 0 & G \end{bmatrix} \begin{bmatrix} \varepsilon_x \\ \varepsilon_y \\ \varepsilon_z \\ \gamma_{yz} \\ \gamma_{zx} \\ \gamma_{xy} \end{bmatrix} \quad (7)$$

Such as:

$$C_{11} = C_{22}, C_{12} = C_{23}, C_{66} = \frac{C_{22}-C_{23}}{2} = \frac{C_{11}-C_{12}}{2} \quad (8)$$

$$C_{11} = \frac{E(1-v)}{(1-2v)(1+v)} \quad (9)$$

$$C_{12} = \frac{vE}{(1-2v)(1+v)} \quad (10)$$

It follows that:

$$G = \frac{E}{2(1+v)} \quad (11)$$

4. Periodic Boundary Conditions (PBC)

Periodic boundary conditions (PBCs) are applied to the representative volume element (RVE) that captures the composite microstructure, as shown in Figure 4. Even for relatively small RVE sizes, these conditions have been shown to yield higher accuracy in computing effective properties [38]. To enforce periodicity, kinematic continuity is imposed between opposite faces of the RVE, mimicking the behavior of an infinite periodic medium. By prescribing a specific displacement relationship between these faces, artificial separation or interpenetration at the boundaries is avoided [39]. The PBCs are mathematically expressed as [40]:

$$u_i = \bar{\varepsilon}_{ij} x_j + v_i \quad (12)$$

The average strain components are represen ted here by $\bar{\varepsilon}_{ij}$, the displacement components of the periodic part are denoted by v_i (local fluctua tion on boundary surfaces), and the displacemen ts of the RVE in x_j directions are represented by u_i. On opposite boundary faces, the displacemen t components are given as:

$$u_i^{n+} = \bar{\varepsilon}_{ij} x_j^{n+} + v_i^{n+} \quad (13)$$

$$u_i^{n-} = \bar{\varepsilon}_{ij} x_j^{n-} + v_i^{n-} \quad (14)$$

where the positive and negative directions along x_j are represented, respectively, by n+ and n-. On opposing boundary faces of the RVE model, the periodic parts of the displacement components v_i^{n+} and v_i^{n-} are the same. Equation (13) minus equation (14) is computed as follows:

$$u_i^{n+} - u_i^{n-} = \bar{\varepsilon}_{ij}\left(x_j^{n+} - x_j^{n-}\right) = \bar{\varepsilon}_{ij}\Delta x_j \quad (15)$$

where Δx_j denotes the edge length of the RVE. For the analysis, the RVE dimensions are set to $a_x = a_y = a_z = 1\text{x}10^{-2}$ m, and an average deformation of 1% is imposed in the direction of the three axes to evaluate the elastic stiffness matrix of the composite. As an illustration, here is the equation giving these periodic boundary conditions:

$$\begin{cases} \bar{u}\ \{face\ (x=0,y,z) = 0;\ \bar{u}\ \{face\ (x=a_x,y,z) = 1\ \} \\ \bar{v}\ \{face\ (x=0,y,z) = 0;\ \bar{w}\ \{face\ (x=0,y,z) = 0\ \} \end{cases} \quad (16)$$

In the context of a periodic microstructure, periodic boundary conditions (PBCs) are applied to ensure that the deformation field is compatible across the RVE boundaries, as if the RVE were embedded in an infinite array of identical cells. Specifically, when a macroscopic strain is imposed, the displacements on opposite faces of the RVE are constrained to satisfy a prescribed relationship (Equation 15), rather than being left free or unloaded. This condition is applied consistently along all coordinate directions. Figure 4 illustrates the pairs of periodic boundary conditions implemented in this study.

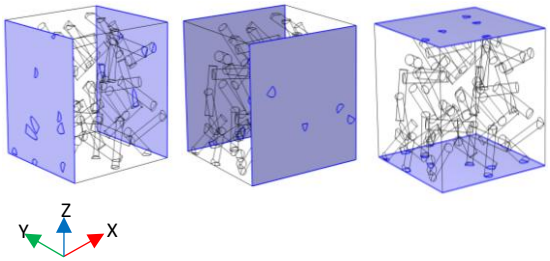

Fig. 4. Boundary pair 1, 2, and 3, respectively, for 5% fiber volume fraction.

When periodic boundary conditions (PBCs) are applied to the representative volume element (RVE) as shown in Table 1, the volume averages of the microscopic stress and strain fields over the RVE correspond exactly to the macroscopic (effective) stress and strain. For a linear elastic composite, this property enables the computation of the effective stiffness tensor at the macroscale through volume averaging. The relationship between the average stress and strain in the RVE is expressed as follows:

$$\bar{\sigma}_{ij} = C^*_{ijkl}\bar{\varepsilon}_{kl} \tag{17}$$

$$\bar{\sigma}_{ij} = \frac{1}{V}\int_V \sigma_{ij}\, dV \tag{18}$$

$$\bar{\varepsilon}_{ij} = \frac{1}{V}\int_V \varepsilon_{ij}\, dV \tag{19}$$

Table 1. Periodic boundary conditions (PBC) applied in the *x*, *y*, and *z* directions on the six faces of the RVE, [41]

		Boundaries					
		Pair 1 (X faces)		**Pair2 (Y faces)**		**Pair 3 (Z faces)**	
Properties	**Constraints**	**X⁻**	**X⁺**	**Y⁻**	**Y⁺**	**Z⁻**	**Z⁺**
E_1 and ν_{12}	u	0	1	Free	Free	Free	Free
	v	Free	Free	0	Free	Free	Free
	w	Free	Free	Free	Free	0	Free
E_2	u	0	Free	Free	Free	Free	Free
	v	Free	Free	0	1	Free	Free
	w	Free	Free	Free	Free	0	Free
E_3	u	0	Free	Free	Free	Free	Free
	v	Free	Free	0	Free	Free	Free
	w	Free	Free	Free	Free	0	1
G	u	0	0	0	0	0	0
	v					0	0
	w			0	0		1

where the average stresses are represented by $\bar{\sigma}_{ij}$ and the average strains by $\bar{\varepsilon}_{ij}$. Periodic RVE volume is denoted by V . The formulation based on finite elements is as follows:

$$\bar{\sigma}_{ij} = \sum_{k=1}^{N} \sigma_{ij}^k V^k \tag{20}$$

$$\bar{\varepsilon}_{ij} = \sum_{k=1}^{N} \varepsilon_{ij}^k V^k \tag{21}$$

where N indicates the total number of finite elements in the RVE model and k is the label of a finite element. The effective elastic properties are estimated by using equations (9), (10), and (11).

5. Analytical Homogenization

The effective elastic properties of heterogeneous materials can be estimated using analytical micromechanical models. These models are based on several key assumptions: (i) both the matrix and inclusions are linearly elastic and isotropic, (ii) the inclusions are symmetric (e.g., spherical, cylindrical, or ellipsoidal), and (iii) perfect bonding exists at the matrix–inclusion interface [42]. Analytical micromechanical models provide formulations of varying complexity and accuracy. Some offer simple closed-form expressions for the effective stiffness (C) and compliance (S) tensors. Among these, the Rule of Mixtures (RoM)—based on the classical bounds proposed by Voigt (1889) and Reuss (1929)—enables straightforward estimation of elastic properties such as (E_{11}, E_{22}, ν_{12} and G_{12}). However, these basic models do not account for inclusion shape, spatial distribution, or orientation, and are therefore limited to idealized microstructures (e.g., aligned continuous fibers for Voigt, or iso-stress assumptions for Reuss). The Halpin–Tsai model was developed to improve the prediction of transverse and shear properties—specifically E_{22} and G_{12} —which the classical Rule of Mixtures (Voigt/Reuss bounds) failed to capture

accurately compared to experimental data. Later, the Chamis model was proposed as a semi-empirical approach that provides reasonable estimates for the five independent elastic constants of unidirectional composites. In this model, the longitudinal modulus E_{11} and major Poisson's ratio v_{12} are calculated using the Rule of Mixtures (ROM), while the remaining three properties E_{22}, G_{12} and G_{23} are evaluated using empirical relations—here given by Eqs. (24), (25), and (26). Among the analytical micromechanical models frequently cited in the literature, the Mori–Tanaka method stands out for its ability to account for interactions between inclusions. A particularly clear and concise formulation of this approach was later provided by Benveniste [43]. Unlike simpler mean-field models (e.g., the Rule of Mixtures), the Mori–Tanaka scheme enables the estimation of macroscopic elastic moduli for composites containing heterogeneities of varying shapes, aspect ratios, orientations, and material properties.

$$E_{11} = V_f E_f + V_m E_m \tag{22}$$

$$\mathrm{v}_{12} = \mathrm{V_f} v_\mathrm{f} + \mathrm{V_m} v_\mathrm{m} \tag{23}$$

$$E_{22} = \frac{E_m}{1 - \sqrt{V_f}\left(1 - {E_m}/{E_f}\right)} \tag{24}$$

$$G_{12} = \frac{G_m}{1 - \sqrt{V_f}\left(1 - {G_m}/{G_f}\right)} \tag{25}$$

$$G_{22} = \frac{G_m}{1 - \sqrt{V_f}\left(1 - {G_m}/{G_f}\right)} \tag{26}$$

where V_f, E_f and v_f denote the fiber volume fraction, Young's modulus, and Poisson's ratio, respectively, and V_m, E_m and v_m represent the corresponding properties of the matrix.

6. Mesh Density

The number of finite elements used to discretize the RVE is referred to as the mesh density. For the mesh convergence study, a 3D microstructure of concrete containing 2% steel fibers by volume is considered, with both the number of fibers and the RVE dimensions held constant. As shown in Figure 5, the variation of the effective Young's modulus with the number of finite elements in the mesh. The modulus initially increases slightly from 28.59 GPa to 28.64 GPa, followed by a minor decrease to 28.46 GPa. As the mesh is further refined, the solution stabilizes, indicating convergence of the effective property. Figure 5 shows that the numerical response stabilizes beyond approximately 40,000 finite elements, indicating mesh convergence. However, the effective shear modulus—plotted as a function of mesh density in Figure 6—exhibits a slight increase from 7.07 GPa to 7.09 GPa, followed by a small but noticeable drop to 7.04 GPa at higher mesh densities. This non-monotonic behavior suggests that while global quantities converge, the computed shear modulus remains sensitive to mesh refinement, possibly due to microstructural randomness or local stress field resolution. Consistent with the global response, the effective shear modulus converges at higher mesh densities: Figure 6 indicates stabilization beyond approximately 67,090 elements.

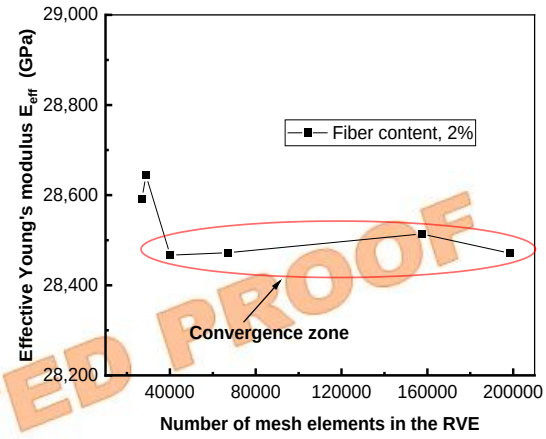

Fig. 5. Convergence of the homogenized Young's modulus with mesh refinement.

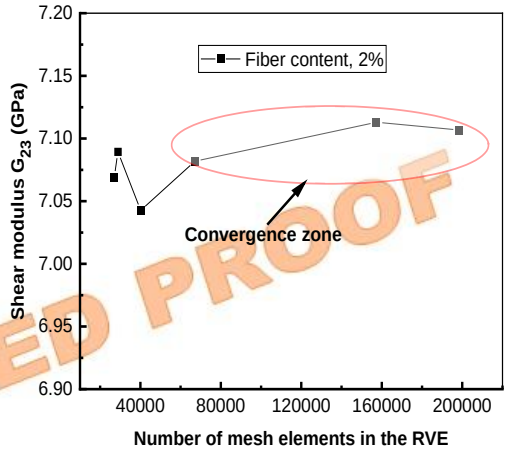

Fig. 6. Convergence of the homogenized shear modulus with mesh refinement.

7. Results and discussions

Both the concrete matrix and the steel fibers (AISI 4340) are assumed to be isotropic and homogeneous. Their mechanical properties are summarized in Table 2.

Table 2. Mechanical properties of constituent materials.

Properties	Units	Concrete	Steel AISI 4340

Density	Kg/m³)	2300	7850
Poisson's ratio		0.20	0.28
Young's modulus	(GPa)	25	205

The numerical results are obtained using a cubic representative volume element (RVE) of dimensions 0.1 × 0.1 × 0.1 m, first without fibers and subsequently with steel fiber volume fractions of 1%, 2%, 5%, 8%, and 10%, as illustrated in Figure 7.

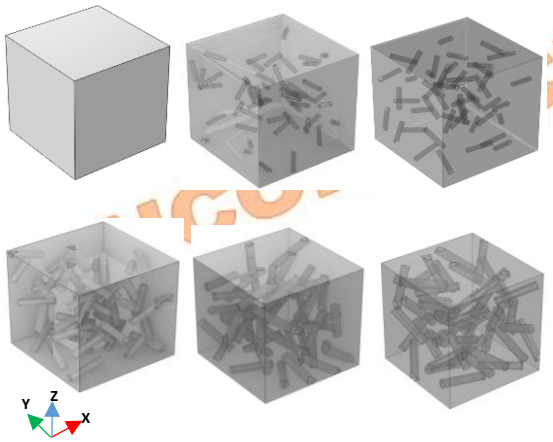

Fig. 7. Variation of fiber volume fraction within the RVE.

7.1. Variation of Effective Young's modulus E_{eff} with the fiber volume fraction.

Increasing the steel fiber volume fraction leads to a progressive rise in the effective Young's modulus, as shown in Figure 8. Under the assumption of perfect interfacial adhesion, which ensures full load transfer, the relationship remains nearly linear, reaching 33.73 GPa at a 10% fiber content. This trend aligns reasonably well with classical micromechanical models: the Chamis prediction (34.61 GPa) slightly overshoots the numerical results, while the Halpin–Tsai model (30.64 GPa) yields a modestly lower prediction.

Crucially, this apparent agreement stems not from the models' ability to capture microstructural reality, but from their shared reliance on idealized assumptions—namely, perfect bonding, uniform stress fields, and the absence of defects. The small residual gap between Chamis model and Halpin–Tsai model, even under these ideal conditions, reveals a deeper distinction: Chamis model treats the composite as a unidirectional laminate with continuous fibers, effectively maximizing reinforcement efficiency, whereas Halpin–Tsai model incorporates an empirical shape factor that implicitly accounts for finite fiber aspect ratio and limited load-transfer length—even when perfect adhesion is assumed. Thus, the slight underprediction of the Halpin–Tsai model may actually reflect a more physically grounded treatment of short-fiber kinematics. In real steel fiber–reinforced concrete, however, interfacial debonding, fiber pull-out, and incomplete embedment are common—especially at higher fiber dosages where workability declines and clustering increases. These mechanisms would significantly attenuate the stiffening effect, causing experimental data to fall below all idealized curves. Consequently, the current agreement should be interpreted not as validation of predictive accuracy, but as confirmation that the simulation framework correctly implements the assumed physics. This underscores a key limitation: the model's applicability is confined to high-bond, low-porosity systems, and it should be used with caution in practical mix designs where interfacial imperfections dominate post-peak behavior.

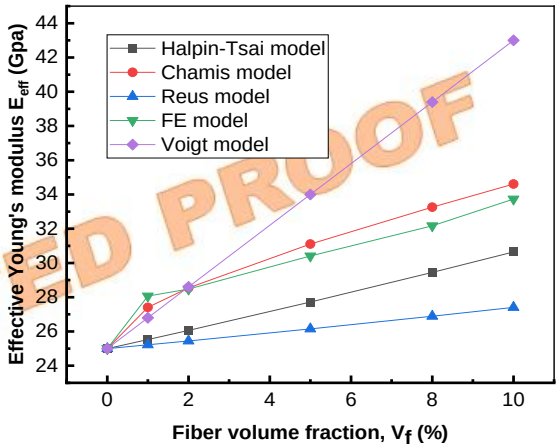

Fig. 8. Variation of the effective Young's modulus with fiber volume fraction.

7.2. Variation of Shear modulus with the fiber volume fraction.

Figure 9 shows that the effective shear modulus of the steel fiber–concrete composite increases nearly linearly with fiber volume fraction. Among the micromechanical models considered, the Chamis model yields the highest prediction (14.30 GPa at 10% fiber content), significantly exceeding both the numerical RVE result (12.60 GPa) and the estimates from the Voigt (11.41 GPa) and Halpin–Tsai (11.96 GPa) models. This overestimation arises because the Chamis model assumes perfectly aligned fibers, ideal load transfer, and a porosity-free matrix—conditions that do not reflect the random fiber orientation, interfacial imperfections, and microstructural heterogeneity of real steel fiber–reinforced concrete. In contrast, the Halpin–Tsai model, through its empirical shape factor, partially accounts for fiber aspect ratio and orientation, leading to better agreement with RVE simulations. For practical material design

involving randomly distributed short fibers, *the Halpin–Tsai* model offers a reasonable balance between simplicity and physical realism, while RVE-based simulations remain the most reliable for detailed validation. Direct application of the Chamis model in this context is discouraged, as it may lead to non-conservative (overly optimistic) stiffness predictions.

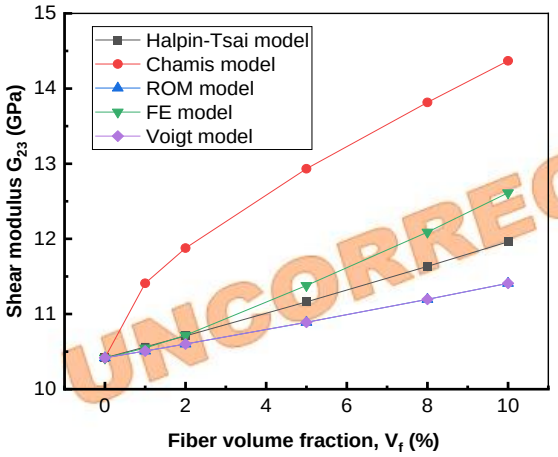

Fig. 9. *Variation of the shear modulus with fiber volume fraction.*

7.3. Variation in the plane of Poisson's ratio on fiber volume fraction.

The numerical model predicts an increase in the effective Poisson's ratio (in the *x-y* plane) with rising steel fiber volume fraction, as illustrated in Figure 10. The rise in the effective Poisson's ratio with fiber content can be explained by the fact that steel fibers exhibit a higher Poisson's ratio than the concrete matrix. In other words, as the steel fiber volume fraction increases, the effective Young's modulus of the composite increases, indicating enhanced stiffness. The comparison with the analytical model of Reuss shows a certain similarity in the values of Poisson's ratio of the concrete/steel composite. At a steel fiber volume fraction of 10%, the numerical prediction of the in-plane Poisson's ratio (0.2075) closely matches the Reuss model estimate (0.2079), with a relative deviation of less than 0.2%.

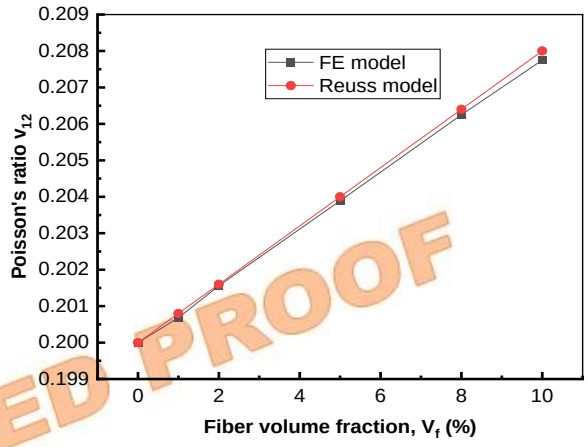

Fig. 10. Variation of Poisson's ratio with fiber volume fraction

7.4. Variation of effective Young's modulus E_{eff} with a fraction of the volume of the voids.

Analysis of the local fields obtained through numerical homogenization at the scale of the representative volume element (RVE) reveals significant stress concentrations near the fiber–matrix and pore–matrix interfaces, as shown in Figure 11. Peaks in the von Mises equivalent stress are localized around the ends of steel fibers and at the edges of spherical pores. Notably, pores adjacent to fibers induce local stress interactions, disrupting the symmetry of the stress fields and intensifying local gradients. These results indicate that, at the microstructural scale, failure initiates in these regions.

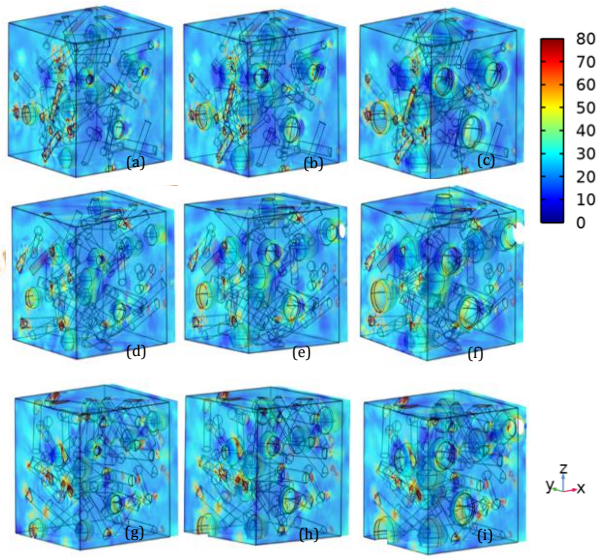

Fig. 11. Stress distribution due to the effective Young's modulus for fiber volume fractions (a,b,c) 5%, (d,e,f) 8% (g,h, i) 10% and voids volume fractions (a,d,g) 2%, (b,e,h) 5%, (c,f, i) 8%

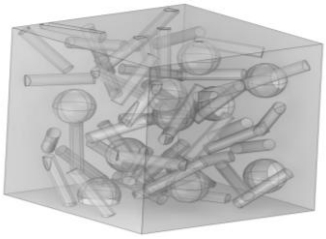

Fig. 12. RVE with void volume fraction, V_v(%).

The predicted effective Young's modulus of the composite is shown in Figure 12 for steel fiber volume fractions of 5%, 8%, and 10%, each evaluated across void volume fractions of 0%, 2%, 5%, and 8%. The predicted results confirm that the effective Young's modulus of the concrete–steel fiber composite decreases with increasing void volume fraction. This reflects the expected softening effect of porosity: as void content rises, the composite's stiffness declines. Figure 13 shows that, for a steel fiber volume fraction of 10%, the effective Young's modulus of the concrete–steel fiber composite decreases from 33.73 GPa (0% voids) to 29.24 GPa (8% voids), i.e., a reduction of approximately 13.30% due to 8% porosity. The longitudinal Young's modulus increases from 29.09 GPa (5% fiber, 2% voids) to 32.29 GPa (10% fiber, 2% voids)—an 11% increase—highlighting the stiffening effect of higher fiber content under constant porosity. Conversely, at fixed fiber content (10%), increasing the void fraction from 2% to 10% reduces the modulus from 32.29 GPa to 29.24 GPa, a 9.5% decrease, underscoring the detrimental role of porosity.

The mean longitudinal modulus rises from 28.44 GPa (95% CI: [25.38, 31.50] GPa) at 5% fiber content to 31.59 GPa (95% CI: [28.72, 34.45] GPa) at 10%, confirming that the stiffening effect is not only consistent but also statistically significant—the confidence intervals show limited overlap, suggesting a robust dependence on fiber volume fraction.

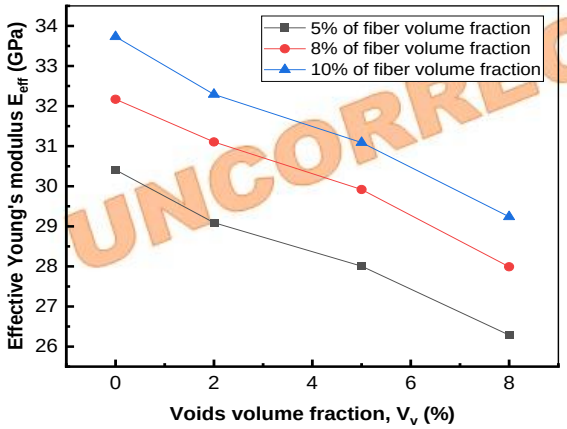

Fig. 13. Variation of the effective modulus with void volume fraction

7.5. Variation of shear modulus G_{23} with a fraction volume of voids.

Figure 14 shows that at the RVE scale, numerical homogenization reveals strong stress concentrations near fiber–matrix and pore–matrix interfaces, with von Mises stress peaks at fiber tips and pore edges. Pores adjacent to fibers induce asymmetric stress fields and steeper gradients, indicating that microscale failure preferentially initiates in these zones.

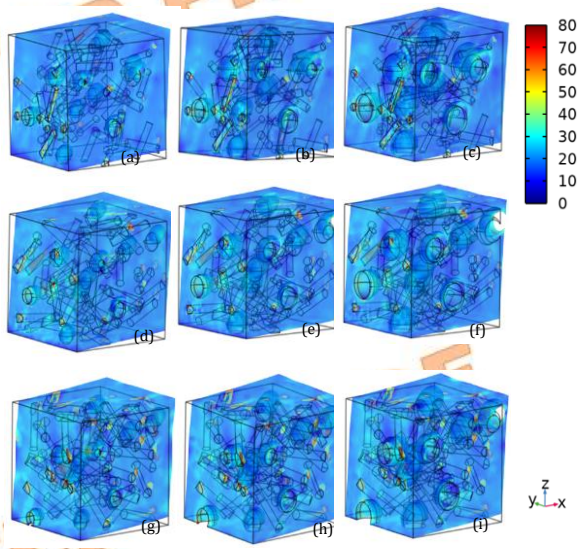

Fig. 14. Stress distribution due to the shear modulus for fiber volume fractions (a,b,c) 5%, (d,e,f) 8% (g,h, i) 10% and voids volume fractions (a,d,g) 2%, (b,e,h) 5%, (c,f, i) 8%

Figure 15 shows the predicted values of the shear modulus of the composite in the y–z plane, with void volume fractions of 0%, 2%, 5%, and 8%. The predicted effective shear modulus of the concrete–steel fiber composite decreases linearly as a function of increasing void volume fractions. The greater the percentage of voids, the more the rigidity of the composite decreases. In other words, the stiffness of the composite also decreases as the void content in the matrix increases. As shown in Figure 15, for a fiber volume fraction of 10%, the shear modulus of the concrete–steel fiber composite drops from 12.61 GPa (with 0% voids) to 10.92 GPa at a void volume fraction of 8%. The curve shows that the shear modulus increases from 10.98 GPa (5% fiber with 2% voids) to 12.13 GPa (10% fiber with 2% voids), corresponding to an increase of approximately 10.47%. Conversely, it decreases from 12.13 GPa (10% fiber with 2% voids) to 10.92 GPa (10% fiber with 10% voids), representing a reduction of about 9.98% in the shear modulus. The mean shear modulus is 10.69 GPa for a fiber volume fraction of 5%, with a 95% confidence interval of [9.56, 11.82] GPa. At 10% fiber volume fraction, the mean Young's

modulus increases to 11.82 GPa, with a 95% confidence interval of [10.81, 12.83] GPa.

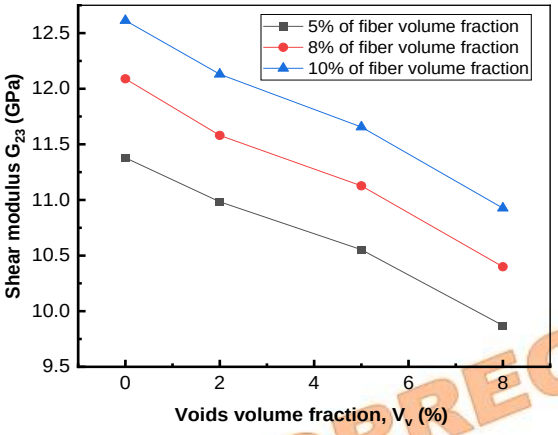

Fig. 15. Variation of the shear modulus with void volume fraction

7.6. Effect of the length-to-diameter ratio of the cylindrical fibers

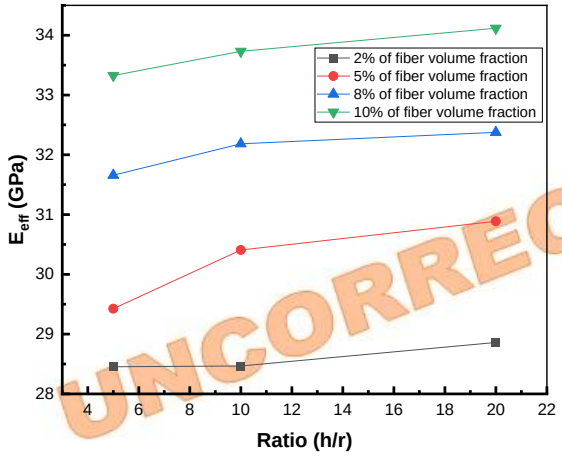

Fig. 16. Effective elastic modulus as a function of the fiber length-to-diameter aspect ratio (h/r).

The fiber length-to-diameter ratio (h/r) directly influences the composite's stiffness: increasing h/r leads to a progressive rise in the effective Young's modulus. At a fixed fiber volume fraction of 8 %, the effective modulus increases from 31.66 GPa (h/r = 5) to 32.18 GPa (h/r = 10) and reaches 32.37 GPa (h/r = 20), confirming that longer fibers enhance stiffness. These findings support the use of longer fibers (higher h/r) over shorter fibers, particularly when stiffness is a primary design criterion.

8. Conclusions

The present study evaluated the effective elastic properties of a concrete composite reinforced with cylindrical steel fibers at fiber volume fractions of 0%, 1%, 2%, 5%, 8%, and 10% using the finite element method (FEM) in conjunction with a numerical homogenization technique. The study accounted for the length-to-diameter ratio of the cylindrical fibers by fixing the number of fibers at 50. Three cases were considered: (1) fiber length equal to five times the diameter, (2) ten times the diameter, and (3) twenty times the diameter. Additionally, the effect of concrete porosity was evaluated by varying the void volume fraction at 2%, 5%, and 8%. All the results obtained were compared and validated against analytical predictions, including the Halpin–Tsai, Chamis, Reuss, RoM, and Voigt models. The present work does not aim to demonstrate the dominant contribution of fibers to pre-cracking stiffness, which is already well-established in the literature. Rather, its novelty lies in the RVE-based numerical homogenization framework that simultaneously incorporates randomly distributed fibers and voids under periodic boundary conditions, and in the systematic investigation of their coupled effects on the effective elastic properties.

Using the representative volume element (RVE) model, the predicted effective properties show close agreement with analytical predictions, with a deviation in Poisson's ratio of no more than 2.47 %. This indicates that the proposed methodology effectively and accurately captures the mechanical behavior of composite materials. Furthermore, this technique can be extended to other composite architectures—such as long-fiber–reinforced or woven-fiber–reinforced composites—While numerical homogenization offers a powerful complement to experimental testing—enabling parametric exploration and microstructural insight at reduced cost—it cannot yet replace physical characterization for certification or safety-critical applications. Key limitations include: (i) sensitivity to uncertain interfacial properties (e.g., fiber–matrix bond), (ii) idealized assumptions in RVE generation (e.g., random fiber distribution vs. real casting-induced orientation), and (iii) absence of time-dependent or damage-coupled effects in the present elastic framework. Experimental validation remains essential to ground-truth model predictions. The numerical computations carried out on the concrete–steel fiber composite developed in this study yielded the following results:

- A stabilization is observed for a high mesh density. Respectively, from 40,000 and 67,090 elements, a stabilization of the value of Young's and shear moduli begins to be observed.
- Increasing the steel fiber volume fraction directly enhances the effective Young's and shear moduli, thereby increasing the composite's rigidity. Conversely, the presence of voids in the

concrete matrix significantly reduces these effective properties.

- The analytical homogenization method (AHM) used to estimate the effective elastic properties demonstrates that analytical models are an effective tool for predicting the mechanical behavior of composites at the selected steel fiber volume fractions.
- By adopting a numerical homogenization approach based on the finite element method (FEM) and a Representative Volume Element (RVE), the effective elastic properties of the composite were estimated. These numerical results show very good agreement with those obtained from analytical computations.
- Numerical homogenization simulations reveal that mechanical discontinuities at interfaces—particularly between fibers and the matrix, or around pores—give rise to localized regions of high stress concentration, a critical mechanism in the initiation of failure.
- Increasing fiber length enhances composite stiffness, thereby justifying the preferential use of higher-aspect-ratio fibers (h/r)—especially in stiffness-driven design contexts.

The assumption of perfect bonding between the cementitious matrix and fibers is a common simplification in linear elastic micromechanical modeling. While it facilitates analytical tractability and reduces computational cost, this idealization overlooks critical interfacial phenomena observed in real fiber-reinforced concrete. In practice, the fiber–matrix interface is often compromised by microstructural defects—such as interfacial porosity, incomplete fiber embedment, weak chemical adhesion (especially with smooth steel or untreated synthetic fibers), or microcracking during curing. These imperfections reduce stress-transfer efficiency and can lead to localized slip or early debonding under load. As a result, models assuming perfect adhesion tend to overestimate effective stiffness and underestimate strain capacity, particularly beyond the elastic regime. Although acceptable for preliminary elastic predictions under low loading, this assumption becomes increasingly unrealistic when assessing post-peak behavior, toughness, or long-term durability—highlighting the need for more advanced interfacial models (e.g., cohesive zone models or frictional contact formulations).

Conflicts of Interest

The author declares that there is no conflict of interest regarding the publication of this manuscript.

References

[1] Shahjalal, Md. Islam, K. Batool, F. Tiznobaik, M. Zahid Hossain, F.M. Sakil Ahmed, Kh. Shahria Alam, M. Ahsan, R., 2023. Fiber-reinforced recycled aggregate concrete with crumb rubber: A state-of-the-art review, Construction and Building Materials, 404 133233.

[2] Verian, K.P. Ashraf, W. Cao, Y., 2018. Properties of recycled concrete aggregate and their influence in new concrete production, Resour. Conserv. Recycl. 133, pp. 30–49.

[3] De Almeida Ferreira, I.C. Paciornika, S. De Andrade Silva, F., 2024. Microstructural investigation of concretes with recycled aggregates using X-ray microtomography, Journal of Building Engineering, 84 108487.

[4] Vega-Pava, O. Torrente-Prato, G., 2023. Flexural strength increases of concrete with AISI 4140 steel chip as reinforcement, Construction and Building Materials, 407 133512.

[5] Chu, H. Gao, S. Gao, L. An, Y. Jiang, J., 2023. Effects of steel chips on the microstructure, mechanical property, and durability of ultra-high-performance concrete with high elastic modulus, Journal of Building Engineering, 72 106662.

[6] Hurtado-Figueroa, O. Varum, H. Prieto, M.I. Amaya, R.J.G. Escamilla, A.C., 2025. Effect of fiber-matrix interaction and embedment length on the pullout behavior of rice straw fibers embedded in clay matrix, Results in Engineering, 27 106144.

[7] Sudin, R. Swamy, N., 2006. Bamboo and wood fibre cement composites for sustainable infrastructure regeneration. J. Mater. Sci. 2006, 41(21), pp. 6917–6924.

[8] Page, J. Sonebi, M. Amziane, S., 2017. Design and multi-physical properties of a new hybrid hemp-flax composite material. Constr. Build. Mater. 139, pp. 502–512.

[9] Bhowmik, R. Das, S. Mallick, D. Gautam, S.S., 2022. Predicting the elastic properties of hemp fiber – A comparative study on different polymer composite, Material Today : Procedings, 50(5), pp. 2510-2514.

[10] Momoh, E.O. Osofero, A.I., 2020. Recent developments in the application of oil palm

fibers in cement composites. Front. Struct. Civ. Eng. 14, pp. 94–108.

[11] Souidi, A. Atigui, M. Maaloufa, Y. Amazal, M. Oubeddou, S. Mounir, S. Aharoune, A., 2024. Comparative stady of Gybsum Composite Materials reinforced with Date Palm and Polyester Fibres. Revue des Composites et des Matériaux Avancés-Journal of Composite and Advanced Materials, 34(2), pp.133-142. doi/10.18280/rcma.340202.

[12] Page, J. Amziane, S. Gomina, M. Djelal, C., 2021. Audonnet, F. Using linseed oil as flax fibre coating for fibre-reinforced cementitious composite. Industrial Crops and Product, 161 113168.

[13] Sadeghzade, M. Gharehbaghi, H. Farrokhabadi, A., 2021. Experimental and analytical studies of mechanical properties of additively manufactured lattice structure based on octagonal bipyramid cubic unit cell, Additive Manufacturing, 48 102403.

[14] Gharehbaghi, H. Sadeghzade, M. Farrokhabadi, A., 2022. Introducing the new lattice structure based on the representative element double octagonal bipyramid, Aerospace Science and Technology, 121 107383.

[15] Hussain Gharehbaghi, H. Farrokhabadi, A., 2024. Experimental, analytical, and numerical studies of the energy absorption capacity of bi-material lattice structures based on quadrilateral bipyramid unit cell, Composite Structures, 337 118042.

[16] Gharehbaghi, H., Farrokhabadi, A., & Noroozi, Z., 2023. Introducing a new hybrid surface strut-based lattice structure with enhanced energy absorption capacity. *Mechanics of Advanced Materials and Structures*, *31*(14), pp. 2955–2964. doi.org/10.1080/15376494.2023.2167246.

[17] Gharehbaghi, H., Farrokhabadi, A., 2023. Analytical, experimental, and numerical evaluation of mechanical properties of a new unit cell with hyperbolic shear deformable beam theory. *Mechanics of Advanced Materials and Structures*, *31*(25), pp. 6419–6433.

[18] Ghalehney, S.M. Sadeghi, M.H. Barati, H. and Gharehbaghi, H., 2024. Enhancing auxetic gradient structures for hip joint implants to optimize stress shielding reduction, Phys.Scr, 99 115941. doi 10.1088/1402-4896/ad818e.

[19] Omairey, Sadik L. Dunning, Peter D. Sriramula, S., 2019. Development of an ABAQUS plugin tool for periodic RVE homogenisation, Engineering with Computers, 35, pp. 567–577.

[20] Tian, W. Qi, L. Liang, J. Chao, X. Zhou, J., 2015. Evaluation for elastic properties of metal matrix composites with randomly distributed fibers: Two-step mean-field homogenization procedure versus FE homogenization method, Journal of Alloys and Compounds, 658, pp. 241-247. doi: 10.1016/j.jallcom.2015.10.190.

[21] Cao, Yuzhe, 2016. Representative Volume Element (RVE) Finite-Element Analysis (FEA) of Al Metal-matrix Composites. *Theses and Dissertations*. 1256. https://dc.uwm.edu/etd/1256.

[22] Liu, H. Zeng,Yang Li, D. Jiang, L., 2016. Development of RVE-embedded solide elements model for predicting effective elastic constants of discontinuous fiber reinforced composites. Mechanics of Materials, 93, pp. 109–123.

[23] Rao Devireddy, S.B. Biswas, S., 2014. Effect of Fiber Geometry and Representative Volume Element on Elastic and Thermal Properties of Unidirectional Fiber-Reinforced Composites, Journal of Composites, Volume 2014, Article ID 629175.

[24] Xu, L. Huang, Y., 2017. Effects of Voids on Concrete Tensile Fracturing: A Mesoscale Study, Advances in Materials Science and Engineering, Volume 2017, Article ID 7989346.

[25] Elminor, H. Bahraoui, I. Hilali, E. Elminor, H., 2016. The Effective Elastic Properties And The RVE Size By Satatistic And Numerical Approach For Porous Materials, Journal of Mechanical and Civil Engineering (IOSR-JMCE) 2278-1684, 13(3), pp. 118-126.

[26] Eshelby, J.D., 1957. The Determination of the Elastic Field of an Ellipsoidal Inclusion, and Related Problems. Proceedings of the Royal Society of London A: Mathematical, Physical and Engineering Sciences, 241(1226), pp. 376-396.

[27] Hill, R., 1963. Elastic Properties of Reinforced Solids: Some Theoretical Principles. Journal of the Mechanics and Physics of Solids, 11(5), pp. 357-372.

[28] Hashin, Z. Shtrikman, S., 1963. A Variational Approach to the Theory of the Elastic Behaviour of Multiphase Materials. Journal of the Mechanics and Physics of Solids, 11(2), pp. 127-140.

[29] Mori T, Tanaka K., 1973. Average stress in matrix and average elastic energy of materials with misfitting inclusions, Acta Mettall. 21, pp. 571-574.

[30] Voigt W., 1889. Uber die Beziehung zwischen den beiden Elastizitatskonstanten Isotroper Korper. Wied. Ann, 38, pp. 573-587.

[31] Reuss A., 1929. Berechnung der Fliessgrense von Mischkristallen auf Grund der Plastizitätsbedingung für Einkristalle. Zeitschrift Angewandte Mathematik und Mechanik, 9, pp. 49-58.

[32] Chamis CC., 1989. Mechanics of composite materials: past, present, and future. J Compos Technol Res ASTM 1989, 11, pp. 3–14.

[33] Fedotov, A.F., 2022. Mori-Tanaka experimental-analytical model for predicting engineering elastic moduli of composite materials, Composites Part B: Engineering, 232 109635.

[34] Kumar, A. DasGupta, A. Jain, A., 2024. Microstructure generation algorithm and micromechanics of curved fiber composites with random waviness. International Journal of Solids and Structures, 289 112625.

[35] Okereke, M.I. Ling, Y., 2018. A computational investigation of the effect of three-dimensional void morphology on the thermal resistance of solder thermal interface materials. Applied Thermal Engineering, 142, pp. 346-360.

[36] Barbero, E.J., 2013. Finite element analysis of composite materials using Abaqus, 2013. https://books.google.com/books?hl=en&lr=&id=sKHT0WwTm2UC&pgis=1.

[37] Kaw, Autar K., 2006. Mechanics of composite materials / Autar K. Kaw. 2nd ed. p. cm. (Mechanical engineering ; v. 29) Includes bibliographical references and index. ISBN 0-8493-1343-0. by Taylor & Francis Group, LLC.

[38] Choi S, Sankar BV., 2006. Micromechanical Analysis of Composite Laminates at Cryogenic Temperatures. Journal of Composite Materials, 40(12), pp. 1077-1091. doi:10.1177/0021998305057365

[39] Hollister, S.J., Kikuchi, N., 1992. A comparison of homogenization and standard mechanics analyses for periodic porous composites. Computational Mechanics, 10, pp. 73–95. doi.org/10.1007/BF00369853

[40] K Jagath Narayana and Ramesh Gupta Burela, 2019. Multi-scale modeling and simulation of natural fiber reinforced composites (Bio-composites), J. Phys.: Conf. Ser. 1240(1) 012103. doi 10.1088/1742-6596/1240/1/012103

[41] Agwu, N., Ozoegwu, C. G., Ugwu, C. O., & Jacobs, I. O., 2021. Finite element estimation of the effective mechanical properties of coir fiber-reinforced high-density polyethylene. Mechanics of Advanced Materials and Structures, 29(26), pp. 4942–4951. doi.org/10.1080/15376494.2021.1943080

[42] Ting, T.C.T. Schiavone, P., 2010. Uniform antiplane shear stress inside an anisotropic elastic inclusion of arbitrary shape with perfect or imperfect interface bonding, International Journal of Engineering Science, 48 pp. 67-77. https://doi.org/10.1016/j.ijengsci.2009.06.008.

[43] Benveniste, Y., 1987. A new approach to the application of Mori-Tanaka's theory in com posite materials », *Mech. Mater.*, 6(2), pp. 147-157.